High-frequency dynamics of liquid and supercritical water

F. Bencivenga,[1] A. Cunsolo,[2] M. Krisch,[3] G. Monaco,[3] G. Ruocco,[4] and F. Sette[3]
[1]*Sincrotrone Trieste, S.S. 14 km 163.5 in Area, Science Park, I-34012 Basovizza, Trieste, Italy*
[2]*CRS SOFT-INFM-CNR-Operative Group in Grenoble, c/o ILL, Boîte Postale 220, F-38043 Grenoble, Cedex, France*
[3]*European Synchrotron Radiation Facility, Boîte Postale 220, F-38043 Grenoble, Cedex, France*
[4]*Dipartimento di Fisica and CRS SOFT-INFM-CNR, Universitá di Roma "La Sapienza," Roma, Italy*
(Received 18 December 2006; revised manuscript received 16 March 2007; published 15 May 2007)

The dynamic structure factor $S(Q,\omega)$ of water has been determined by high-resolution inelastic x-ray scattering (IXS) in a momentum (Q) and energy (E) transfer range extending from 2 to 4 nm^{-1} and from ±40 meV. IXS spectra have been recorded along an isobaric path (400 bar) in a temperature (T) interval ranging from ambient up to supercritical ($T>647$ K) conditions. The experimental data have been described in the frame of the generalized hydrodynamic theory, utilizing a model based on the memory function approach. This model allows identifying the active relaxation processes which affect the time decay of density fluctuations, as well as a direct determination of the Q, T, and density (ρ) dependencies of the involved transport parameters. The experimental spectra are well described by considering three different relaxation processes: the thermal, the structural, and the instantaneous one. On approaching supercritical conditions, we observe that the microscopic mechanism responsible for the structural relaxation is no longer related to the making and breaking of intermolecular bonds, but to binary intermolecular collisions.

DOI: 10.1103/PhysRevE.75.051202 PACS number(s): 61.20.−p, 63.50.+x, 61.10.Eq, 62.60.+v

I. INTRODUCTION

Water plays a unique role in natural science and technology. Despite its apparent chemical simplicity, water presents various physical anomalies whose origin still eludes a comprehensive explanation [1]. Owing to the relevance of the subject and the fundamental nature of the unresolved puzzles, water still represents a challenge for researchers in various disciplines. There is an almost unanimous consensus in ascribing the origin of the water peculiarities to the almost perfect tetrahedral arrangement of molecules, as well as to the occurrence of a 1:1 donor-to-acceptor ratio of hydrogen bonds (HB). These features favor the formation of a highly ordered local structure that continuously rearranges itself on a sub-ps time scale. Consequently, experimental investigations of the THz dynamics of water promise to provide valuable insight.

Direct access to this dynamical range is provided, from the computational side, by molecular dynamics (MD) simulations, and, from the experimental one, by high-frequency spectroscopies such as inelastic neutron (INS) or x-ray (IXS) scattering. All MD [2–4], INS [5–9], and IXS [10–16] investigations performed so far on liquid water showed the existence of propagating collective excitations with wave vectors (Q) in the nm^{-1} range and characteristic energies [$\hbar\Omega_L(Q)$] much larger than what was predicted by the classical hydrodynamic theory for longitudinal acoustic (LA) modes [17]. This effect was ascribed either to a coupling between an optical and an acoustic branch [8,9], or to the occurrence of an active structural (α) relaxation, similar to the one observed in glass-forming systems [13–16]. Such a relaxation yields, as a most spectacular effect, the Q increase of the propagation speed of LA modes (positive sound dispersion). Actually, the latter framework has proven to provide a more coherent explanation of the Q and T dependencies of this phenomenon. The idea at the basis of such a model relies upon the existence of two opposite regimes characterizing the dynamical response of the system: i.e., the viscous and the elastic one. The viscous regime is probed whenever an acoustic wave with a period, $T_L=\Omega_L^{-1}(Q)$, much longer than the time scale τ_α of the relaxation process is excited. Under these conditions the system behaves like a viscous fluid as predicted by the classical hydrodynamics theory. Conversely, when the period of the acoustic wave becomes much shorter than τ_α, the dynamic response enters into the elastic regime. Here, such short time scales are probed that the medium appears somehow "frozen," like in the corresponding glass. Its internal degrees of freedom become too slow to efficiently dissipate the energy of the acoustic wave, and consequently the sound velocity is higher than in the viscous regime.

Most of the theoretical models developed to describe this (viscoelastic) transition relied on the hypothesis that the hydrodynamic equations can be safely extended beyond the viscous limit, provided the transport coefficients are generalized as appropriate ω-dependent quantities. A model belonging to such a "generalized hydrodynamics" class has been successfully tested to describe the line shape of IXS spectra [14] of water. Among other results the work showed that τ_α follows an Arrhenius behavior with an activation threshold comparable to the HB energy throughout the whole liquid phase. This evidence strongly supports the hypothesis that the microscopic mechanism responsible for the relaxation process is indeed the continuous rearrangements of the water HB network.

In this work we present new, high resolution IXS measurements extending the thermodynamic range so far investigated by IXS, into the supercritical regime of the phase diagram ($T_c=647$ K, $P_c=221$ bar, and $\rho_c=322$ kg/m^3). Though IXS studies of water along the liquid-to-supercritical crossover are reported in literature [18], no firm experimental hints are so far available on the corresponding evolution of

active relaxations. To gain a deeper insight into this topic, we propose here a more informative line-shape analysis based on the memory function formalism, thus providing a full characterization of relaxations active in water. As a result, we find that viscoelastic effects on the acoustic dispersion gradually disappear by going from liquid to supercritical conditions, and, correspondingly, the temperature dependence of τ_α deviates from the Arrhenius law typical of the liquid phase. The latter effect reveals major changes in the nature of the involved relaxation, which in the liquid phase is dominated by collective arrangements, while in the supercritical region becomes essentially governed by binary intermolecular collisions.

The paper is organized as follows. In Sec. II we introduce the employed experimental technique and mention the relevant experimental details. In Sec. III we illustrate the formalism used for the data analysis, and in Sec. IV the fitting procedure is described. The main results of the data analysis are extensively discussed in Sec. V. Finally, Sec. VI summarizes the relevant results and provides the conclusions.

II. EXPERIMENT

The experiment was carried out at the inelastic scattering beamline ID28 of the ESRF at Grenoble (France). The x-ray source consists of three undulators tuned to optimize the photon flux at 21.747 keV. After a premonochromatization ($\Delta E/E \sim 10^{-4}$), achieved by a cryogenically cooled channel cut silicon(1,1,1) monochromator, the x-ray beam impinges on the very high-resolution backscattering monochromator, which is operated at a Bragg angle of 89.98°, and employs the silicon(11,11,11) reflection order. The backscattered x rays have an energy resolution of $\approx$1.1 meV ($\Delta E/E = 6 \times 10^{-8}$) with a photon flux of 4×10^9 photons/s [19]. This highly monochromatic beam is focused onto the sample by a gold coated toroidal mirror, yielding a focal spot size of 270×90 μm^2 (horizontal $\times$ vertical, FWHM) at the sample position. The signal scattered from the sample is energy analyzed by five independent spherical silicon crystals, employing the same reflection order and approximately the same Bragg angle as the monochromator, that are mounted at the end of the 7-m-long spectrometer arm [20]. This arm can be rotated around a vertical axis passing through the scattering center in order to select the desired momentum transfer $Q = 2k_i \sin(\theta)$, where 2θ and k_i are the scattering angle and the incident wave vector, respectively. The angular offset between adjacent analyzers is $\sim$1.5°, corresponding to a Q offset of $\sim$3 nm^{-1} for the chosen incident energy. The momentum resolution was set to 0.4 nm^{-1} FWHM by slits in front of the analyzers. The energy-analyzed x rays are detected by a Peltier cooled array of silicon detectors [21]. The overall experimental resolution was determined to be 1.6 meV FWHM, using the essentially elastic scattering response of a PMMA sample at its first sharp diffraction peak (10 nm^{-1}), and at $T = 10$ K. For each thermodynamic state a measurement of the static structure factor $S(Q)$ of the sample was performed using an additional detector, mounted on the spectrometer arm. A detailed description of the spectrometer is reported elsewhere [22].

Ultrapure water was loaded in a specially designed high-pressure, high-temperature, large volume cell made of Inconel 625 [23]. The sample was pressurized by a manually driven piston and thermoregulated by means of a resistor. The maximum pressure and temperature achievable are 1 kbar and 750 K, respectively. The temperature and pressure stability were monitored by a thermocouple and two pressure gauges, and were found to be better than ±0.2 K and ±5 bar, respectively. The x-ray beam passes through two 1-mm-thick diamond windows kept at 10-mm distance, roughly matching the photoabsorption length of water. The whole setup was kept under vacuum in order to avoid temperature gradients and scattering from air surrounding the cell.

The energy dependence of the empty cell intensity was explicitly measured for all the exploited scattering geometries. The highest value is reached at the lowest Q value (i.e., 2 nm^{-1}) and it amounts to 1.5% of the total scattered signal. This contribution rapidly decreases with increasing Q, and has therefore been simply discarded in the line-shape analysis. The results of the empty cell measurements, corrected by the X-ray attenuation through the water sample ($I/I_0 \approx 0.45$), are reported in Fig. 2 (open circles), and compared to the total measured signal after a proper scaling for the incident photon flux.

In order to derive the true $S(Q,\omega)$ from the raw data, we assumed that the background mainly comes from two distinct contributions: the electronic noise ($\approx$0.002 Hz) and the sample environment. Both are supposed to have a flat energy distribution within the narrow frequency window explored here. The overall background contribution was experimentally determined by recording the $S(Q,\omega)$ in the high-frequency region (60–100 meV) on the anti-Stokes side of the spectrum, where no contribution from the water vibrational spectrum was observed. These measurements have been repeated for all scattering geometries employed in the experiment. The recorded signal ($\approx$1–4 counts/min, depending on the scattering angle) can be safely taken as a reliable measure of the global background. Moreover, it is worthwhile mentioning that we performed parallel fitting sessions for some representative spectra keeping the background fixed to different values. This procedure revealed that ±50% variations of the experimentally determined background value did not change the values of the other fit parameters within the error bars.

Multiple scattering contributions were evaluated following the same route as in Ref. [14] and were found to be less than 2% of the total measured signal.

These results make us confident that the measured signal is essentially the dynamical structure factor $S(Q,\omega)$ of water convoluted with the instrumental resolution function. During the experiment the pressure was kept fixed ($P = 400$ bar), and the temperature was changed between 293 and 706 K. The investigated thermodynamic states are reported in Table I, together with the corresponding values of some thermodynamic quantities.

For each thermodynamic state we collected at least 10 IXS spectra in the 2–14 nm^{-1} Q range. The typical energy transfer region was ±40 meV, with an integration time rang-

TABLE I. Relevant properties of the investigated thermodynamic states at $P=400$ bar: temperature T, density ρ, adiabatic sound velocity c_s, specific heat ratio γ, thermal diffusivity D_T, and kinematic shear viscosity ν_s.

T (K)	ρ (kg/m^3)	c_s (m/s)	γ	D_T (cm^2/s)	ν_s (cm^2/s)
293	1016	1548	1.01	14.9×10^4	98×10^4
337	998	1625	1.06	16.5×10^4	45×10^4
367	980	1628	1.1	17.2×10^4	31.8×10^4
398	958	1602	1.15	17.7×10^4	24.3×10^4
423	938	1565	1.2	18×10^4	20.5×10^4
447	917	1519	1.25	18.1×10^4	18×10^4
494	869	1400	1.36	17.9×10^4	15×10^4
549	800	1220	1.53	16.9×10^4	13.1×10^4
598	719	1013	1.77	14.9×10^4	12.1×10^4
660	573	707	2.55	10.5×10^4	11.7×10^4
706	348	495	4.32	6.32×10^4	12.8×10^4

ing from 70 to 140 s. In parallel to the IXS measurements we also collected the energy integrated signal $I(Q)$ as a function of Q in the 1–24 nm^{-1} range, using a silicon detector with an energy resolution of 600 eV.

III. THEORETICAL FORMALISM

The line shape of the IXS spectra was described using a phenomenological line-shape model, derived in the frame of the memory function formalism. In recent years this approach was successfully employed to describe the IXS spectra of many disordered systems such as water [13,14,16] and other hydrogen bonded liquids [24–26], noble gasses [27], liquid metals [28], diatomic liquids [29], supercooled molecular systems [30], and glasses [31]. In this framework the time dependence of the intermediate scattering function $F(Q,t)$ can be expressed in terms of the so-called first-order memory function $m_1(Q,t)$ [32,33]. Moreover, it is possible to iterate the procedure and express the t dependence of $m_1(Q,t)$ in terms of another function called the second-order memory function $m_2(Q,t)$, and so on. This iterative formalism is synthesized in the continued fraction representation for $F(Q,t)$ [32,33] as follows:

$$\frac{\tilde{F}(Q,s)}{F(Q,0)} = \left[s + \frac{\Delta_1}{s + \dfrac{\Delta_2}{s + \dfrac{\Delta_3}{s + \cdots}}} \right]^{-1}, \tag{1}$$

where $\tilde{F}(Q,s)$ is the Laplace transform of $F(Q,t)$, $F(Q,0)=S(Q)$ and Δ_n are quantities that can be expressed in terms of the spectral momenta of order $i \leqslant n$. Truncating the development of Eq. (1) at the second order we obtain

$$\frac{\tilde{F}(Q,s)}{S(Q)} = \left[s + \frac{\Omega_T^2(Q)}{s + \tilde{m}(Q,s)} \right]^{-1}, \tag{2}$$

where $\tilde{m}(Q,s)$ is the Laplace transform of the second-order memory function $m_2(Q,t)$, and $\Omega_T(Q)=\sqrt{\Delta_1}$ is the isothermal sound frequency, which is linked to $S(Q)$ through the finite-Q generalization of the compressibility theorem [32,33] as follows:

$$\Omega_T^2(Q) = \frac{k_B T Q^2}{M S(Q)}, \tag{3}$$

where k_B is the Boltzmann constant, T is the absolute temperature, and M is the molecular mass. The variable measured in an IXS experiment is the dynamical structure factor $S(Q,\omega)$, which is readily obtained from Eq. (2) using the relation between Laplace and Fourier transforms as follows:

$$\begin{aligned} \frac{S(Q,\omega)}{S(Q)} &= \frac{1}{\pi} \mathrm{Im}\left[\tilde{F}(Q,s)/S(Q)\right]_{s=i\omega} \\ &= \frac{1}{\pi} \frac{\Omega_T^2(Q) m'(Q,\omega)}{\left[\omega^2 - \Omega_T^2(Q) - \omega m''(Q,\omega)\right]^2 + \left[\omega m'(Q,\omega)\right]^2}, \end{aligned} \tag{4}$$

where $m'(Q,\omega)$ and $m''(Q,\omega)$ are the real and imaginary parts of the time Fourier transform of $m_2(Q,t)$, respectively. The specific choice to truncate Eq. (1) at the second order represents a good compromise between a fully satisfactory description of the experimental data and a rather simple analytical expression for $S(Q,\omega)$. Further developments of the continued fraction representation beyond the second order formally ensure the automatic fulfilment of higher-order sum rules [32,33]. As a consequence, a better description of $S(Q,\omega)$ in the spectral tail region could be provided. However, such a more accurate approximation is well beyond the accuracy of the present data.

1. Memory function in the hydrodynamic limit

The information concerning the dynamics of the system is contained in the memory function $m_2(Q,t)$ [hereafter we will indicate $m_2(Q,t)$ as $m(Q,t)$]. It is therefore crucial to carefully choose an appropriate functional form for $m(Q,t)$. The

expression reported in Eq. (5) allows keeping consistency with the classical hydrodynamic theory in the low Q limit [32] as follows:

$$m(Q,t) = 2\nu_L Q^2 \delta(t) + (\gamma - 1)\Omega_T^2(Q) e^{-D_T Q^2 t}, \tag{5}$$

where γ and ν_L are the specific heat ratio and the longitudinal kinematic viscosity, respectively, $D_T = \lambda/\rho C_V$ is the thermal diffusion coefficient, and ρ, λ, and C_V are the density, the thermal conductivity, and the specific heat at constant volume, respectively. In fact, inserting the Fourier transform of Eq. (5) into Eq. (4), one obtains

$$\frac{S(Q,\omega)}{S(Q)} = \frac{1}{\pi} \frac{\Omega_T^2(Q)\Gamma_L(\omega)}{[\omega^2 - \Omega_L^2(\omega)]^2 + [\omega\Gamma_L(\omega)]^2}. \tag{6}$$

Here $\Omega_L^2(\omega) = \Omega_T^2(Q) + (\gamma - 1)\Omega_T^2(Q) y^2/(1+y^2)$ and $\Gamma_L(\omega) = \nu_L Q^2 + (\gamma - 1)\Omega_T^2(Q)/D_T Q^2(1+y^2)$, where we have introduced the dimensionless variable $y = \omega/D_T Q^2$.

Within the hydrodynamic limit, i.e., for $D_T Q^2$ and $\nu_L Q^2 \ll \Omega_L(\omega) = cQ$ (with c the sound velocity), Eq. (6) reduces to the well known Rayleigh-Brillouin spectrum. In this limit inelastic modes in the spectrum account for the existence of density waves having a propagation speed $\sqrt{\gamma}\Omega_T(Q) = \sqrt{\gamma} c_T Q = c_s Q$, where c_T and c_s are the isothermal and adiabatic sound velocity, respectively.

2. Transition between the adiabatic and the isothermal regimes

From a physical point of view the hydrodynamic constraint $D_T Q^2 \ll \Omega_L(Q)$ implies that thermal diffusion is much slower than the period of the acoustic wave, which therefore propagates without thermal exchanges—i.e., adiabatically—through the medium. With increasing Q, the period of the acoustic modes (Ω_L^{-1}) decreases as Q^{-1}, while the time scale of thermal diffusion $(\tau_T = 1/D_T Q^2)$ decreases as Q^{-2}. As a consequence, at sufficiently large Q values the inequality $D_T Q^2 \gg \Omega_L(Q)$ (i.e., $y \ll 1$) is fulfilled, and thermal exchanges become fast enough to thermalize the acoustic wave within a propagation period. Taking the $y \ll 1$ limit of Eq. (6), it can be noticed that the effective sound frequency (Ω_L) reduces to the isothermal rather than the adiabatic one. Briefly, the finite time decay of the memory function induced by thermal diffusion leads to a modification of the sound velocity, consisting of an adiabatic to isothermal transition of sound propagation around the crossover condition $\Omega_L(Q) \approx \tau_T^{-1}(Q)$.

3. Memory function beyond the hydrodynamic limit

The term $\propto \delta(t)$ in Eq. (5) accounts for the viscous contribution to the damping of LA modes. The related time decay appears as instantaneous only in the long time-scale (hydrodynamic) limit. However, if the dynamic response is probed within the THz range, as for IXS experiments, this instantaneous approximation definitely breaks down. One of the most popular ansatz to describe the behavior of the memory function in this regime is to split the instantaneous contribution into two terms [10–14,16]: (a) An exponential decay with time-constant τ_α in the order of ~ps; (b) a fast contribution $\propto \delta(t)$, taking into account both ultrafast dynamical events (e.g., intramolecular vibrations) [34,35], and the effect of topological disorder [31]. With this ansatz Eq. (6) becomes

$$m(Q,t) = 2\Gamma_\mu(Q)\delta(t) + \Delta_\alpha^2(Q) e^{-t/\tau_\alpha(Q)} + [\gamma(Q) - 1]\Omega_T^2(Q) e^{-D_T(Q)Q^2 t}, \tag{7}$$

where

$$\Delta_\alpha^2(Q) = [c_\infty^2(Q) - c_s^2(Q)]Q^2 \tag{8}$$

is the strength of the structural relaxation. In Eq. (7) all the parameters are taken as Q-dependent generalizations of the corresponding macroscopic variables. Finally, in order to allow Eq. (7) to be consistent with Eq. (5) in the hydrodynamic limit, the following constraint has to be superimposed:

$$\nu_L(Q)Q^2 = \Delta_\alpha^2(Q)\tau_\alpha(Q) + \Gamma_\mu(Q). \tag{9}$$

4. Viscoelastic transition

The presence of the first exponential term in Eq. (7) allows retrieving the mentioned viscoelastic transition, responsible for the positive sound dispersion. In fact, this term gives rise to a frequency dependence of the hypersonic parameters Ω_L^2 and Γ_L^2 in Eq. (6), namely,

$$\Omega_L^2 = \Omega_T^2(Q) + (\gamma - 1)\Omega_T^2(Q) y^2/(1+y^2) + [c_\infty^2(Q) - c_s^2(Q)]Q^2(Q)x^2/(1+x^2), \tag{10}$$

and

$$\Gamma_L = (\gamma - 1)\Omega_T^2(Q)\tau_T(Q)/(1+y^2) + [c_\infty^2(Q) - c_s^2(Q)]Q^2\tau_\alpha(Q)/(1+x^2) + \Gamma_\mu(Q), \tag{11}$$

where we have introduced the dimensionless variable $x = \omega\tau_\alpha(Q)$. If we neglect, for the sake of simplicity, the effect of thermal relaxations, i.e., setting $\gamma = 1$, we observe that the resulting $S(Q,\omega)$ is characterized by three distinct dynamical regimes, according to the value of x:

(i) If $x \ll 1$ (viscous regime) the line shape reduces to

$$\frac{S(Q,\omega)}{S(Q)} \sim \frac{1}{\pi} \frac{\Omega_T^2(Q)\nu_L(Q)Q^2}{[\omega^2 - \Omega_T^2(Q)]^2 + [\omega\nu_L(Q)Q^2]^2}, \tag{12}$$

where Eq. (9) has been used. The above expression is fully consistent with the expected hydrodynamic result in the case of $\gamma = 1$, i.e., $c_s = c_T$. It can be shown that such a consistency holds also for $\gamma > 1$ [17].

(ii) When $x \sim 1$ (viscoelastic regime) the propagation speed $[\Omega_L(Q)/Q]$ and damping $[\Gamma_L(Q)/Q^2]$ of LA modes strongly deviate from the hydrodynamic values given by $c_T(Q) = \Omega_T(Q)/Q$ and $\nu_L(Q)$, respectively. More specifically, while increasing x, $\Omega_L(Q)/Q$ increases with respect to $\Omega_T(Q)/Q$ and $\Gamma_L(Q)$ decreases with respect to $\nu_L(Q)$. At the same time a further Lorentzian-type mode appears in the spectrum at $\omega = 0$. Its integrated intensity and half width half maximum reduces to $f(Q) = \Delta_\alpha^2(Q)/(c_\infty(Q)Q)^2$ and $\tau_C^{-1}(Q) = \tau_\alpha^{-1}(Q)c_s^2(Q)/c_\infty^2(Q)$, respectively. These two variables are customarily referred to as the nonergodicity factor and the compliance relaxation time, respectively.

(iii) Finally, when $x \gg 1$ (elastic regime), the line shape becomes

$$\frac{S(Q,\omega)}{S(Q)} \sim f(Q)\delta(\omega) + \frac{1}{\pi}\frac{\Omega_\infty^2(Q)\Gamma_\mu(Q)}{[\omega^2 - \Omega_\infty^2(Q)]^2 + [\omega\Gamma_\mu(Q)]^2}. \tag{13}$$

In this limit, the velocity and damping of LA modes reach again a frequency-independent value given by $c_\infty(Q) = \Omega_\infty(Q)/Q > c_T(Q)$ and $\Gamma_\mu(Q) < \nu_L(Q)Q^2$. Moreover, a fraction of the total spectral density [i.e., $f(Q)$] is confined within a very small frequency window around $\omega=0$.

IV. FITTING PROCEDURE

The IXS spectra $I(Q,\omega)$ were analyzed by a fitting routine based on a standard χ^2 minimization [36] of the following model function:

$$I(Q,\omega) = A(Q)[h(\omega,T)S(Q,\omega) \otimes R(\omega)] + B, \tag{14}$$

where $S(Q,\omega)$ is obtained by inserting the Fourier transform of Eq. (7) into Eq. (4). In Eq. (14), $R(\omega)$ is the measured instrumental resolution function, the symbol $\otimes$ is the convolution operator, A is an overall scaling factor, and B is a background term, taking into account both the electronic background of the detectors and the environmental one. Finally, $h(\omega,T)$ is the dimensionless factor

$$h(\omega,T) = \frac{\hbar\omega/k_BT}{1 - e^{-(\hbar\omega/k_BT)}}, \tag{15}$$

which accounts for the quantum nature of the energy exchanges on a microscopic level, and allows retrieving the asymmetry of the line shape due to the detailed balance principle. In order to reduce the correlation between fitting parameters entering Eq. (14), some of them have been kept fixed, namely, (i) the background B and the temperature T have been fixed to the respective measured values, (ii) both the specific heat ratio $\gamma(Q)$ and the thermal relaxation time $\tau_T(Q)$ were fixed to the values derived from the water equation of state (EoS) [37], and, moreover, were assumed to be Q independent. This choice was motivated by the lack of computational or experimental results for both variables over the rather large thermodynamic range explored by the experiment.

As a result, five parameters were left free to vary without any constraint: (i) the overall intensity factor A; (ii) the Q-dependent generalization of the isothermal sound frequency $\Omega_T(Q)$; (iii) the infinite-frequency sound frequency $\Omega_\infty(Q)$; (iv) the time scale of the exponential relaxation $\tau_\alpha(Q)$; (v) the amplitude of the instantaneous relaxation $\Gamma_\mu(Q)$.

Finally, the characteristic frequency of the LA mode $\Omega_L(Q)$ was evaluated from the maximum position of the longitudinal current spectrum as follows:

$$J_L(Q,\omega) = (\omega/Q)^2 S(Q,\omega), \tag{16}$$

as determined using the best fit line shape $S(Q,\omega)$.

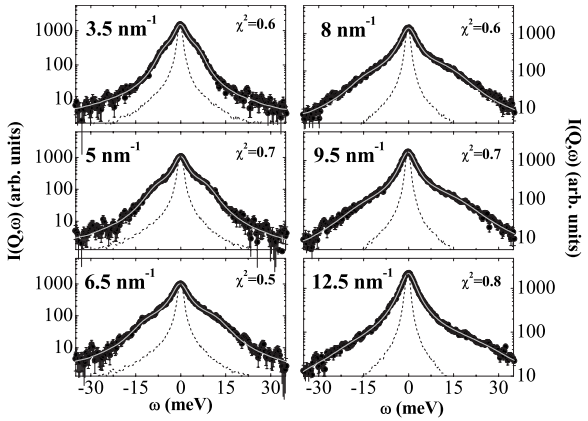

FIG. 1. Selection of IXS spectra of liquid water at $T=367$ K and $P=400$ bar at the momentum transfers indicated in the individual panels. The experimental spectra (full circles) are compared with their corresponding best fit results (solid gray lines) and the instrumental resolution function (dotted black line). The logarithmic scale emphasizes the overall good agreement even in the spectral tails.

In order to better motivate our choice of the data analysis strategy, two further comments are deserved:

(i) The single time-scale decay assumption inherent to the viscoelastic ansatz may appear a rather crude approximation in view of the more realistic hypothesis of a continuous distribution of time scales [38]. However, the introduction of more complex functions in the model would lead to stronger correlations between the various line-shape parameters without improving the quality of the fits.

(ii) In this context, the presence of a second weakly dispersive excitation (experimentally observed at low E's and relatively high Q's [8,9,12,16]) has been discarded, since its spectral contribution is expected to vanish at the rather high T's and low Q's probed by the present experiment. This choice was further supported by an alternative fitting procedure for which a second excitation, empirically described by a damped harmonic oscillator (DHO) function, was added in the model line shape. For temperatures lower than 398 K we found that the integrated intensity (I_2) of the weakly dispersive mode is lower than 10% of the total scattered signal for all the reported Q values, i.e., for $Q < 11$ nm^{-1}. Furthermore, with increasing temperature above ambient conditions I_2 tends to vanish at low Q. At 398 K and above, I_2 was found to be always consistent with zero within the experimental accuracy throughout the explored Q range. Moreover, in all cases the best fit results of the other parameters remained unchanged, thus suggesting that this second excitation indeed does not need to be taken into account in the present case.

Figures 1–4 show a selection of IXS spectra, together with the experimental resolution function and the best fit result. The logarithmic scale in Figs. 1 and 3 emphasizes the excellent agreement even in the tails of the spectra. It is worthwhile recalling that a reliable description of these tails is mandatory to achieve a correct evaluation of the maximum position of the longitudinal current spectrum. The IXS spectra in Fig. 1 clearly reveal distinguishable inelastic features, corresponding to LA modes, whose position shifts towards

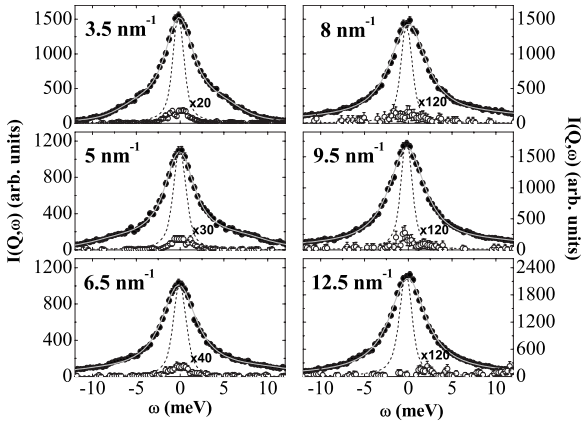

FIG. 2. Central portion of the IXS spectra, reported in Fig. 1, on a linear scale. The open circles correspond to the empty cell contribution, whose intensity has been magnified by the factor indicated in the individual panels.

higher energies with increasing Q. This observation is particularly true for the spectra at $Q<8$ nm^{-1}. For the temperature-dependent IXS spectra at fixed Q (see Fig. 3) the inelastic features become less pronounced with increasing temperature, and any relic of distinct inelastic shoulders in the $S(Q,\omega)$ disappears, likely due to the reduction of the sound velocity on approaching supercritical conditions.

Figure 5 shows representative spectra of the static structure factor measurements. The intensity increase at low Q is due to an increase of long-distance correlations, as expected on approaching critical conditions. Correspondingly, the relative intensity of the first sharp diffraction peak (FSDP) decreases owing to the gradual loss of first neighbor correlations while going towards the gas phase. In order to cast these measurements into absolute units, the measured signal $I(Q)$ has been corrected for the detector background, the atomic scattering factors [39], and geometrical effects. Finally, the intensity was normalized to fulfill the compressibility theorem in the $Q=0$ limit, $S(0)=\rho\chi_T k_B T/M$, where χ_T

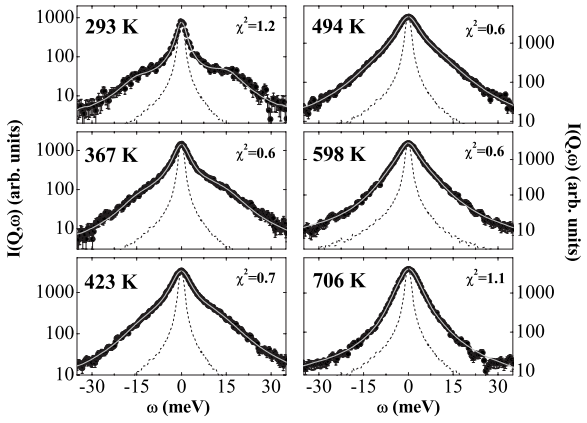

FIG. 3. Selection of IXS spectra of liquid water at $Q=8$ nm^{-1} and $P=400$ bar at the indicated temperatures. The experimental spectra (full circles) are compared with their corresponding best fit results (solid gray lines) and the instrumental resolution function (dotted black line). The logarithmic scale emphasizes the overall good agreement even in the spectral tails.

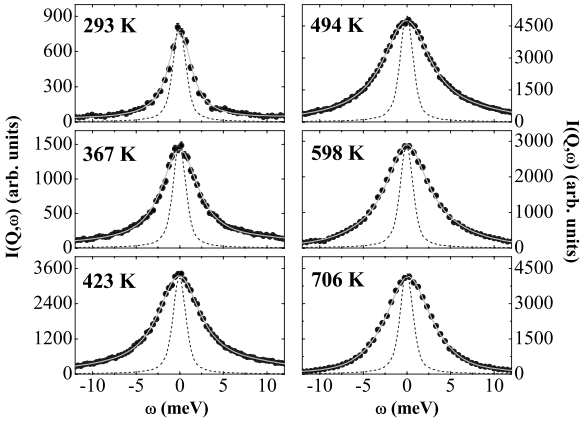

FIG. 4. Central portion of the IXS spectra, reported in Fig. 3, on a linear scale.

and k_B are the isothermal compressibility and the Boltzmann constant, respectively.

V. RESULTS AND DISCUSSION

A. Sound dispersions

Figure 6 reports for some selected thermodynamic states (i) the apparent sound dispersion $\Omega_L(Q)$ corresponding to the maxima of the longitudinal current spectra [Eq. (16)], (ii) the isothermal dispersion $\Omega_T(Q)$ obtained from the fit, or, alternatively, by inserting the experimental values for $S(Q)$ in Eq. (3), (iii) the adiabatic dispersion $\gamma^{1/2}\Omega_T(Q)$, assuming that γ does not depend on Q, (iv) the infinite-frequency dispersion $\Omega_\infty(Q)$, and (v) the inverse of the structural relaxation time $\tau_\alpha^{-1}(Q)$ obtained by interpolation of the fit results (see Fig. 10).

The good agreement between the two independent determinations of the isothermal dispersions provides an important consistency check for the reliability of the fitting procedure. Inspecting Fig. 6(a), it can be observed that the experimental data for $\Omega_L(Q)$ are systematically higher than the ones corresponding to the adiabatic dispersion, and es-

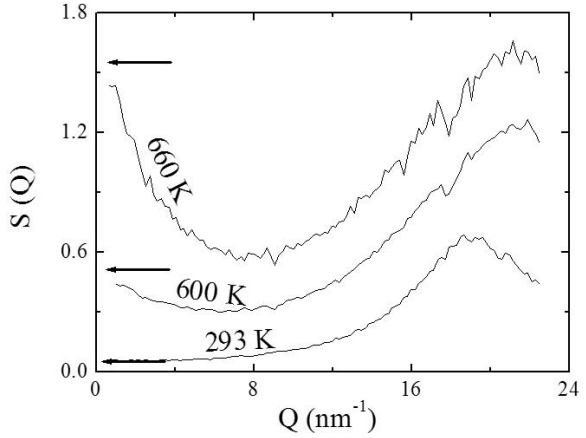

FIG. 5. $S(Q)$ of water at the indicated temperatures. The arrows show the $Q=0$ limit, as evaluated from the water EoS.

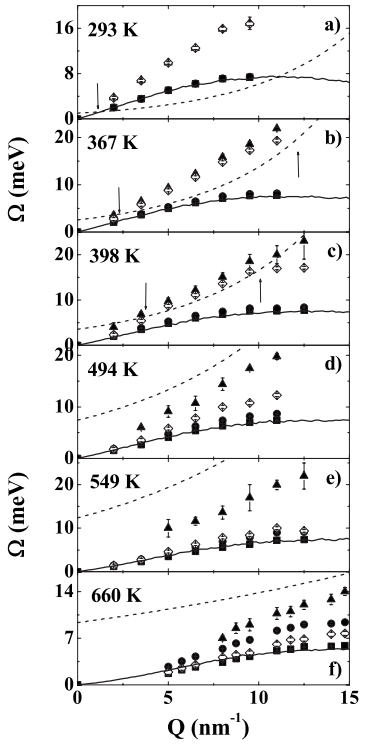

FIG. 6. Comparison between isothermal (squares), adiabatic (circles), infinite (triangles), and apparent longitudinal sound dispersion (open diamonds) at the temperatures indicated in the figure. The isothermal dispersion derived from the experimental S(Q) is reported as well (solid line). The dashed lines indicate the values of $1/\tau_\alpha(Q)$, obtained from the interpolation of the fit results (see Fig. 10). The vertical arrows indicate the crossover condition: $\tau_\alpha^{-1}(Q) \sim \Omega_L(Q)$.

sentially coincide with the infinite-frequency sound dispersion over the explored Q range. This suggests that the viscoelastic transition occurs definitely below the probed Q window at this temperature. With increasing temperature [i.e., from Fig. 6(b)–6(d)], the reported LA dispersions join the respective adiabatic ones at the lowest Q's. On increasing Q, $\Omega_L(Q)$ systematically departs from the hydrodynamic expectation $[\Omega_s(Q)]$ and eventually reaches $\Omega_\infty(Q)$ (positive sound dispersion). Such a viscoelastic transition apparently occurs around the expected crossover position: $\tau_\alpha(Q)\Omega_L(Q) \sim 1$, also shown by vertical arrows. In some cases the viscoelastic crossover is again met at higher Q, due to the lower value of both $\Omega_L(Q)$ and $\tau_\alpha(Q)$. This gives rise to an "inverse" transition, i.e., from the elastic back to the viscous regimes [see, e.g., Fig. 6(c)]. On a general ground, we remark that $\tau_\alpha^{-1}(Q)$ increases with increasing T, while $\Omega_L(Q)$ instead decreases. As a consequence, the viscoelastic condition can never be met at the highest T's and no positive dispersion is observed. This trend is most evident at 549 K [Fig. 6(e)], where $\Omega_L(Q)$ and $\Omega_s(Q)$ essentially coincide.

Briefly, looking at the sequence ranging from Fig. 6(a)–6(e) a gradual disappearance of the positive sound dispersion is observed on approaching T_c. This is consistent with an earlier observation in deeply supercritical Neon [27].

Furthermore, it can be readily noticed from Fig. 6 that $\Omega_\infty(Q)$ has an almost linear Q dependence for $Q < 8$ nm^{-1}. A

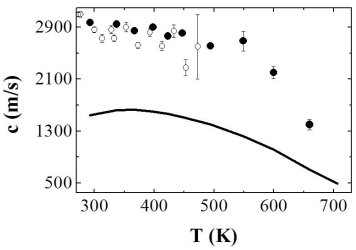

FIG. 7. Temperature dependence of the infinite-frequency sound velocity (full circles) compared with results from Ref. [14] (open circles) and the value of c_s obtained from the water EoS (full line).

linear fit therefore allows the straightforward extraction of the infinite frequency sound speed c_∞ as follows:

$$\Omega_\infty(Q) = c_\infty Q. \tag{17}$$

These values are reported in Fig. 7 as a function of temperature, and compared with the respective values of the adiabatic sound velocity derived from the water EoS [37]. It can be readily noticed that the amplitude of the dispersive step, i.e., the difference between c_∞ and c_s, reduces on going towards supercritical conditions. This is consistent with previous experimental evidences on the reduction of the positive sound dispersion while going towards nearly critical conditions [14,18].

A careful inspection of Figs. 6(e) and 6(f) reveals that another dispersive effect shows up at the highest T's: the adiabatic-to-isothermal transition of sound propagation induced by the thermal diffusion process [29]. In fact we note that $\Omega_L(Q)$ is systematically lower than $\Omega_s(Q)$, and approaches the isothermal values $\Omega_T(Q)$.

In order to achieve a more quantitative characterization of this effect, the following variable is introduced:

$$\Omega_L'(Q) = \Omega_L(Q)\sqrt{1 - \frac{[\Omega_\infty^2(Q) - \Omega_s^2(Q)]\tau_\alpha^2(Q)}{1 + \Omega_L^2(Q)\tau_\alpha^2(Q)}}. \tag{18}$$

It is worthwhile noting that $\Omega_L'(Q)$ is virtually exempt from any viscoelastic dispersive effect [embodied in the Lorentzian term on the right hand side of Eq. (18)], which is explicitly subtracted. Moreover, we introduce the function

$$M_T(Q) = [\Omega_L'^2(Q) - \Omega_s^2(Q)]/[\Omega_T^2(Q) - \Omega_s^2(Q)]. \tag{19}$$

It is readily seen that M_T allows the determination of the isothermal or adiabatic character of the sound dispersion. In fact, $M_T(Q)=0$ or 1 when $\Omega_L'(Q)=\Omega_T(Q)$ or $\Omega_s(Q)$, while $M_T(Q)=0.5$, when $\Omega_L'(Q)\tau_T(Q)=1$.

In Fig. 8 experimental values of M_T are plotted as a function of the dimensionless variable $\Omega_L'(Q)\tau_T(Q)$, derived from the best fits, and compared with the corresponding theoretical prediction. A fair consistency between theoretical and experimental values is appreciated. Minor discrepancies are likely due to the Q dependencies of the parameters $\gamma(Q)$ and $D_T(Q)$, which have been discarded in the present context.

B. Structural relaxation

The viscous contribution to the time decay of the memory function is determined by two parameters, its amplitude

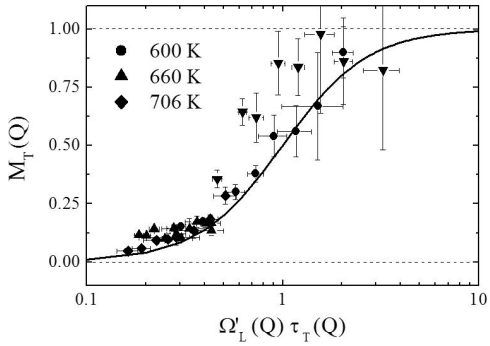

FIG. 8. $M_T(Q)$ as a function of $\Omega_L'(Q)\tau_T(Q)$. The full line represents the expected trend.

$\Delta_\alpha^2(Q)=[c_\infty^2(Q)-c_s^2(Q)]Q^2$, and its time scale $\tau_\alpha(Q)$. Both of them can be derived from the line-shape analysis. With a reasonable ansatz for their Q dependence, their $Q=0$ (macroscopic) limiting values can be obtained by extrapolation. The macroscopic limit of $\Delta_\alpha^2(Q)$ is related to the corresponding ones of c_∞ and c_s through

$$\Delta_\alpha^2 = \lim_{Q\to 0}[\Delta_\alpha^2(Q)/Q^2] = [c_\infty^2 - c_s^2]. \tag{20}$$

In the present study c_s was derived from the EoS, while c_∞ was determined using Eq. (17). The actual values of Δ_α^2 are reported in Fig. 9 as a function of T. The full line is proportional to the density evolution for the $P=400$ bar isobaric path. We notice that Δ_α^2 decreases with increasing T, and that this trend is correlated with the one of the density.

Following the same procedure as above, the macroscopic limit of the relaxation time scale τ_α was evaluated by fitting $\tau_\alpha(Q)$ with an exponential function as follows:

$$\tau_\alpha(Q) = \tau_\alpha e^{-AQ}. \tag{21}$$

Examples of selected fits are reported in Fig. 10. The corresponding $Q=0$ extrapolations τ_α are reported in Fig. 11 in an Arrhenius plot. As long as the sample is liquid, $\tau_\alpha(T)$ can be described by an Arrhenius law as follows:

$$\tau_\alpha = \tau_0 e^{E_a/k_B T}. \tag{22}$$

The resulting value for the activation energy $E_a = 12.0\pm0.3$ kJ/mole is consistent with the value found by Monaco *et al.* (12.6±0.6 kJ/mole) [14,40]. It is believed that the observed relaxation process is somehow related to the extended network of hydrogen bonds existing in water. The

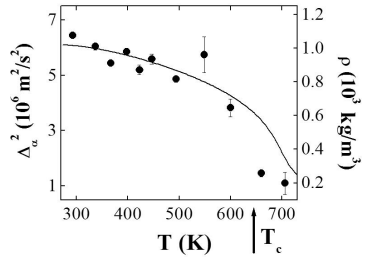

FIG. 9. Δ_α^2 as a function of temperature for $P=400$ bar. The solid line represents the corresponding temperature evolution of the density.

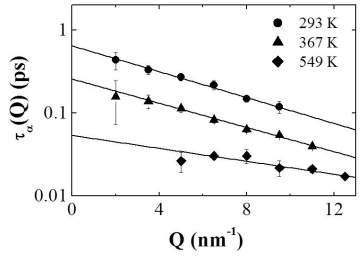

FIG. 10. Q dependence of $\tau_\alpha(Q)$ for some selected temperatures. The lines through the data are linear interpolations using Eq. (21).

principal reasons supporting this picture have been already discussed in Ref. [14]. The main arguments are (i) τ_α is on the same order of the hydrogen bond lifetime and (ii) the activation energy of the relaxation is indeed comparable to the HB energy of water (23 kJ/mole) [1]. Our findings fully support this picture.

In Fig. 11 we compare the present τ_α values with the ones derived from Ref. [14]. One can clearly observe that the two data sets almost coincide despite the rather disparate pressures and densities probed in the two experiments. In a first approximation we can therefore conclude that τ_α does not depend on pressure and density, at least within the relatively low pressure range probed by the two experiments (i.e., $<$ a few kbar).

On approaching the critical temperature the behavior of τ_α deviates from the Arrhenius trend. It is known from diffraction experiments that the structure of the hydrogen bond network in water dramatically changes close to the critical temperature at the relatively low densities investigated here. In particular, the hydrogen bond network structure becomes weaker and the strong tetrahedral coordination of water molecules is substantially lost [41–44]. One can therefore suppose that the departure from the Arrhenius behavior may be correlated to the structural changes that the system undergoes across the liquid-supercritical transition. Moreover, a weakening of the hydrogen bond network around T_c also implies that interactions based on intermolecular bonding are less effective. In this case harsh binary collisions may become the main way to establish interactions among molecules [45]. In order to quantitatively investigate the observed changes in the T dependence of the structural relaxation time, we com-

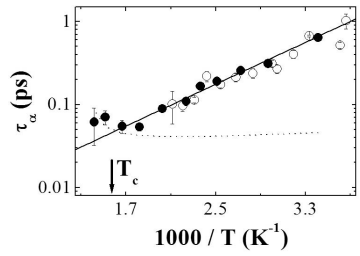

FIG. 11. Arrhenius plot of τ_α (full circles: present work; open circles: Ref. [14]). The full line is the best fit to the experimental data, using Eq. (22), while the dotted one represents the value of $\langle\tau\rangle$, evaluated using Eq. (23). The vertical arrow shows the $1000/T_c$ value.

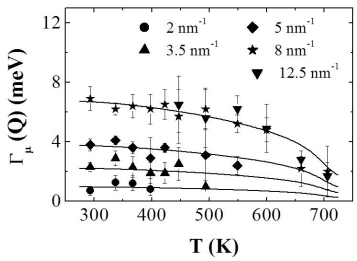

FIG. 12. Temperature dependence of $\Gamma_\mu(Q)$ for some selected Q values. The solid line represents the temperature evolution of the density.

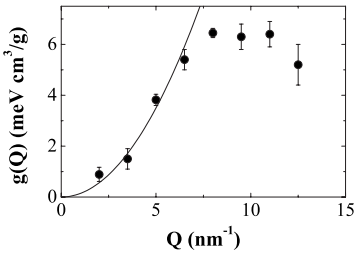

FIG. 13. Average value of the normalized amplitude of the microscopic relaxation, $g(Q)=\Gamma_\mu(Q,T)/\rho(T)$ (see text for further details). The parabola highlights the Q^2 behavior observed in the 0–6.5 nm^{-1} Q range.

pare τ_α with the average microscopic intercollision period $\langle\tau\rangle$ (see Fig. 11). In principle, $\langle\tau\rangle$ is determined by various factors such as molecular size, shape, and mass, as well as by the intermolecular potential and thermodynamic state. However, without sophisticated calculations, a reasonable estimation of $\langle\tau\rangle$ is readily achieved assuming a hard sphere Maxwell-Boltzmann gas (dotted line in Fig. 11) [46] as follows:

$$\langle\tau\rangle = \frac{1}{n}\sqrt{\frac{M}{16\pi d^4 k_B T}}. \tag{23}$$

Here, n and d represent the number density and molecular diameter, respectively. Below T_c, τ_α is much higher than $\langle\tau\rangle$, and most importantly, displays a completely different T evolution. Conversely, τ_α and $\langle\tau\rangle$ become closer on approaching T_c. The interpretation of this phenomenology is rather straightforward: in the liquid phase intermolecular interactions are mainly driven by HB attractions, as assessed by the Arrhenius behavior of τ_α. The lifetime of such a HB interaction sharply decreases with increasing T, and becomes comparable to $\langle\tau\rangle$ close to T_c. Here, the particles can no longer develop an extended network of hydrogen bonds, and mutual interactions become dominated by binary collisions. This peculiar transition between structural and collisional relaxation across the liquid-to-supercritical transition was observed in several systems, and is discussed in detail elsewhere [45].

C. Microscopic relaxation

The microscopic relaxation is induced by dynamical events having time scales τ_μ, much shorter than the probed frequency window. From the analysis of the IXS spectra, the "time integrated" intensity of the corresponding relaxational mode $\Gamma_\mu(Q)$ can be directly evaluated. These values are reported in Fig. 12 as a function of T for some selected Q values. As already observed for Δ^2_α, the T dependence of $\Gamma_\mu(Q)$ is correlated to the one of the density. This observation suggests that there is no explicit T dependence of $\Gamma_\mu(Q)$, in agreement with other literature results [16]. This allows the following factorization of $\Gamma_\mu(Q)$:

$$\Gamma_\mu(Q,T) = g(Q)\rho(T), \tag{24}$$

where $g(Q)$ is an empiric factor insensitive to thermodynamic conditions. In Fig. 13 we report the present values of $g(Q)$ as obtained by averaging $\Gamma_\mu(Q,T)/\rho(T)$ over the probed thermodynamic states. A Q^2 dependence of $g(Q)$ at relatively low Q values can be clearly inferred. This is expected for the viscous damping in the low-Q (hydrodynamic) limit. Furthermore, the data systematically deviate from such quadratic law for increasing Q.

D. Longitudinal viscosity

Finally, the values of the longitudinal viscosity $\eta_L(Q) = \nu_L/Q^2$ were calculated from the fit results through Eq. (9), and are reported in Fig. 14 as a function of Q for some selected temperatures. The lines through the data represent best fit curves obtained within the empirical assumption of an exponential Q decay as follows:

$$\eta_L(Q) = \eta_L e^{-BQ}. \tag{25}$$

The macroscopic ($Q=0$) limit of the longitudinal viscosity η_L can be directly evaluated as best fit parameter. In Fig. 15, the experimental results are reported and compared with the values of the shear viscosity (η_S) extracted from the EoS. In the inset the ratio between the two viscosities is reported. It can be observed that, at least in the liquid phase, this ratio is more or less insensitive to temperature with a value of 4.3±0.2, fully consistent with previous determinations [14,47], thus providing a further check of consistency for the performed data analysis.

VI. CONCLUSIONS

In conclusion we have presented here a concise inelastic x-ray scattering study of the dynamic response of water at

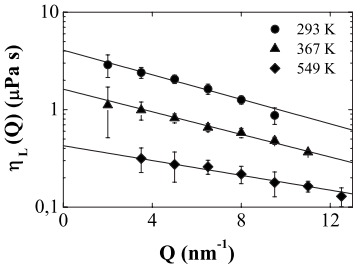

FIG. 14. Q dependence of the longitudinal viscosity $\eta_L(Q)$ for some selected temperatures. The lines through the data are interpolations using Eq. (25).

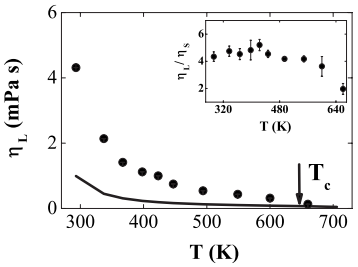

FIG. 15. $Q=0$ extrapolated values of the longitudinal viscosity η_L (full circles), and thermodynamic values of the shear viscosity η_s (solid line), as a function of the temperature. The ratio of the two viscosities is reported in the inset. The vertical arrow indicates the critical temperature.

the transition from the liquid to the supercritical phase. The experimental spectra have been described with a line-shape model derived from the generalized hydrodynamics theory within the assumption that the time decay of the memory function splits into three different terms. The analysis of the T, ρ, and Q dependencies of relevant best fit parameters allows us to draw some very general conclusions concerning the evolution of the high-frequency dynamics across the liquid-supercritical boundary:

(1) Along the whole thermodynamic region explored the Q dispersion of LA modes is influenced by two competing effects, associated to structural and thermal degrees of freedom, respectively. The structural relaxation process dominates in the liquid phase, and it mainly induces a viscoelastic Q transition of the sound propagation, i.e., the well known bending upwards of the dispersion with respect to the hydrodynamic linear behavior. Such dispersive effect tends to disappear on approaching supercritical conditions, where an opposite trend gradually shows up in the form of a negative sound dispersion. Such a feature, predicted by the hydrodynamic theory, physically reveals an adiabatic-to-isothermal transition of sound propagation.

(2) In the liquid phase, the macroscopic limit of the structural relaxation strength (Δ_α^2) is proportional to the density, and in the probed thermodynamic range, it does not explicitly depend on temperature. In the same region, the macroscopic limit of the structural relaxation time follows an Arrhenius behavior, with an activation threshold comparable to the energy of hydrogen bonds, suggesting a close relation between the relaxation and the water hydrogen bond network. However, we believe that a quantitative relationship between the structural relaxation and water structures or interactions cannot be unambiguously assessed on the basis of the present experimental data.

(3) On approaching supercritical conditions, the Arrhenius temperature dependence breaks down and the relaxation time scale becomes similar to the temperature dependence of the characteristic time between intermolecular collisions. This finding suggests that binary intermolecular collisions are dominating the microscopic dynamics in the supercritical phase.

ACKNOWLEDGMENTS

We are grateful to L. Orsingher, D. Gambetti, F. Albergamo, and R. Verbeni for help in the preparation of the experiment.

[1] F. Franks, *Water: A Comprehensive Treatise* (Plenum Press, New York, 1972).
[2] A. Rahman and F. H. Stillinger, Phys. Rev. A **10**, 368 (1974).
[3] U. Balucani, G. Ruoco, A. Torcini, and R. Vallauri, Phys. Rev. E **47**, 1677 (1993).
[4] M. Wojcik and E. Clementi, J. Chem. Phys. **85**, 6085 (1986).
[5] P. Bosi, F. Dupré, F. Menzinger, F. Sacchetti, and M. C. Spinelli, Lett. Nuovo Cimento Soc. Ital. Fis. **21**, 436 (1978).
[6] J. Teixeira, M. C. Bellissent-Funel, S. H. Chen, and B. Dorner, Phys. Rev. Lett. **54**, 2681 (1985).
[7] F. J. Bermejo, M. Alvarez, S. M. Bennington, and R. Vallauri, Phys. Rev. E **51**, 2250 (1995).
[8] C. Petrillo, F. Sacchetti, B. Dorner, and J. B. Suck, Phys. Rev. E **62**, 3611 (2000).
[9] F. Sacchetti, J. B. Suck, C. Petrillo, and B. Dorner, Phys. Rev. E **69**, 061203 (2004).
[10] F. Sette, G. Ruocco, M. Krisch, U. Bergmann, C. Masciovecchio, V. Mazzacurati, G. Signorelli, and R. Verbeni, Phys. Rev. Lett. **75**, 850 (1995).
[11] G. Ruocco and F. Sette, J. Phys.: Condens. Matter **11**, R259 (1999).
[12] F. Sette, G. Ruocco, M. Krisch, C. Masciovecchio, R. Verbeni, and U. Bergmann, Phys. Rev. Lett. **77**, 83 (1996).
[13] A. Cunsolo, G. Ruocco, F. Sette, C. Masciovecchio, A. Mermet, G. Monaco, M. Sampoli, and R. Verbeni, Phys. Rev. Lett. **82**, 775 (1999).
[14] G. Monaco, A. Cunsolo, G. Ruocco, and F. Sette, Phys. Rev. E **60**, 5505 (1999).
[15] M. Krisch, P. Loubeyre, G. Ruocco, F. Sette, A. Cunsolo, M. D'Astuto, R. LeToullec, M. Lorenzen, A. Mermet, G. Monaco, and R. Verbeni, Phys. Rev. Lett. **89**, 125502 (2002).
[16] E. Pontecorvo, M. Krisch, A. Cunsolo, G. Monaco, A. Mermet, R. Verbeni, F. Sette, and G. Ruocco, Phys. Rev. E **71**, 011501 (2005).
[17] B. J. Berne and R. Pecora, *Dynamic Light Scattering* (John Wiley & Sons, New York, 1976).
[18] T. Yamaguchi, K. Yoshida, N. Yamamoto, S. Hosokawa, M. Inui, A. Q. R. Baron, and S. Tsutsui, Nucl. Instrum. Methods Phys. Res. B **238**, 146 (2005).
[19] R. Verbeni, F. Sette, M. Krisch, U. Bergmann, B. Gorges, C. Halcoussis, K. Martel, C. Masciovecchio, J. F. Ribois, G. Ruocco, and H. Sinn, J. Synchrotron Radiat. **3**, 62 (1996).
[20] C. Masciovecchio, U. Bergmann, M. Krisch, G. Ruocco, F. Sette, and R. Verbeni, Nucl. Instrum. Methods Phys. Res. B **117**, 339 (1996).
[21] Canberra Eurisys, Lingolsheim, France.
[22] M. Krisch, J. Raman Spectrosc. **34**, 628 (2003).
[23] Top-Industry, Vaux le Penil, France.

[24] R. Angelini, P. Giura, D. Fioretto, G. Monaco, G. Ruocco, and F. Sette, Phys. Rev. B **70**, 224302 (2004).
[25] G. Monaco, D. Fioretto, C. Masciovecchio, G. Ruocco, and F. Sette, Phys. Rev. Lett. **82**, 1776 (1999).
[26] A. Giugni and A. Cunsolo, J. Phys.: Condens. Matter **18**, 889 (2006).
[27] A. Cunsolo, G. Pratesi, R. Verbeni, D. Colonnesi, C. Masciovecchio, G. Monaco, G. Ruocco, and F. Sette, J. Chem. Phys. **114**, 2259 (2001).
[28] T. Scopigno, G. Ruocco, and F. Sette, Rev. Mod. Phys. **77**, 881 (2005).
[29] F. Bencivenga, A. Cunsolo, M. Krisch, G. Monaco, G. Ruocco, and F. Sette, Europhys. Lett. **75**, 70 (2006).
[30] D. Fioretto, L. Comez, G. Socino, L. Verdini, S. Corezzi, and P. A. Rolla, Phys. Rev. E **59**, 1899 (1999).
[31] G. Ruocco, F. Sette, R. Di Leonardo, G. Monaco, M. Sampoli, T. Scopigno, and G. Viliani, Phys. Rev. Lett. **84**, 5788 (2000).
[32] J. P. Boon and S. Yip, *Molecular Hydrodynamics* (McGraw-Hill International Book Company, New York, 1980).
[33] U. Balucani and M. Zoppi, *Dynamics of the Liquid State* (Clarendon Press, Oxford, 1994).
[34] D. Sette, in *Encyclopedia of Physics*, Vols. Acoustic I and II, edited by S. Flügge (Springer-Verlag, Berlin, 1969).
[35] H. O. Kneser, *Physical Acoustics* (W. P. Mason, New York, 1969).
[36] MINUIT, D516-CERN, Computer 7600, Interim Program Library.
[37] Nist Database, http://webbook.nist.gov/chemistry//formser.html
[38] R. Torre, P. Bartolini, and R. Righini, Nature (London) **428**, 296 (2004).
[39] International tables for x-ray crystallography (Kynoch Press, 1962).
[40] In Ref. [14] the authors report a value of 16 ± 2.5 kJ/mole for the activation energy, as extracted from the Arrhenius temperature depencence of τ_C. The value reported in the text has been instead extracted from the corresponding (Arrhenius) temperature dependence of $\tau_\alpha=\tau_\alpha * c_s^2/c_\infty^2$, where τ_α has been directly calculated from the data reported in Tables I and II of Ref. [14].
[41] A. K. Soper, F. Bruni, and M. A. Ricci, J. Chem. Phys. **106**, 247 (1997).
[42] A. Botti, F. Bruni, M. A. Ricci, and A. K. Soper, J. Chem. Phys. **109**, 3180 (1998).
[43] A. K. Soper, Chem. Phys. **258**, 121 (2000).
[44] J. Marti, Phys. Rev. E **61**, 449 (2000).
[45] F. Bencivenga, A. Cunsolo, M. Krisch, G. Monaco, L. Orsingher, G. Ruocco, F. Sette, and A. Vispa, Phys. Rev. Lett. **98**, 085501 (2007).
[46] J. O. Hirschfelder, C. F. Curtiss, and R. B. Bird, *Molecular Theory of Gases and Liquids* (John Wiley & Sons Inc., New York, 1954).
[47] A. Cunsolo and N. Nardone, J. Chem. Phys. **105**, 3911 (1996).